Physics of Plasmas

Observations of the magneto-Rayleigh-Taylor instability and shock dynamics in gas-puff Z-pinch experiments

Cite as: Phys. Plasmas **25**, 072701 (2018); https://doi.org/10.1063/1.5032084
Submitted: 02 April 2018 . Accepted: 15 June 2018 . Published Online: 10 July 2018

P. W. L. de Grouchy, B. R. Kusse, J. Banasek, J. Engelbrecht, D. A. Hammer, N. Qi, S. Rocco, and S. N. Bland

Observations of the magneto-Rayleigh-Taylor instability and shock dynamics in gas-puff Z-pinch experiments

P. W. L. de Grouchy,[1,2] B. R. Kusse,[1] J. Banasek,[1] J. Engelbrecht,[1,a)] D. A. Hammer,[1] N. Qi,[1,b)] S. Rocco,[1] and S. N. Bland[2]
[1]*Laboratory of Plasma Studies, Cornell University, Ithaca, New York 14853, USA*
[2]*Blackett Laboratory, Imperial College London, London SW7 2AZ, United Kingdom*

(Received 2 April 2018; accepted 15 June 2018; published online 10 July 2018)

We describe a series of experiments performed to study the shock structure generated during the implosion of a gas-puff Z-pinch. The Z-pinch is produced by a double-annular gas-puff with a center jet driven by Cornell University's COBRA generator operating with a 1 MA, 200 ns current pulse. Using 532 nm laser interferometry and 100 MHz multi-frame cameras, a shock structure is observed to form early in the implosion. The shock appears to be created by a current layer at the outer radius of the imploding plasma which acts as a piston moving inward at several hundred km s^{-1}. The dynamics of the shock and its radial position ahead of the piston agree well with a simple uniform density model outlined in the study by Potter [Nucl. Fusion **18**(6), 813 (1978)]. The outer surface of the current layer is observed to be Magneto-Rayleigh-Taylor unstable. The growth rate of this instability is found to depend on the radial density profile of the material within the layer of high-density fluid between the shock and the piston, as predicted by recent theoretical work [see, e.g., D. Livescu, Phys. Fluids **16**(1), 118 (2004)]. Growth rates measured in krypton implosions, where the post-shock material is found to decay quasi-exponentially away from the piston, were more than ten times smaller than those recorded in otherwise identical implosions in argon plasmas, where the material between the shock and the piston was observed to maintain a uniform density. *Published by AIP Publishing.* https://doi.org/10.1063/1.5032084

I. INTRODUCTION

Magnetically driven, cylindrical implosions of high energy density plasmas are a fundamental component of at least two current plasma physics efforts. These are the Magnetized Liner Inertial Fusion (MagLIF) project at Sandia National Laboratories (Slutz, 2012) and the gas-puff Z-pinch experiments used as intense X-ray and neutron sources (Giuliani and Commisso, 2015). In both these cases, large axial currents of 1–25 MA on the outer surface of a cylindrical plasma column drive the implosion. This paper concerns two phenomena that are present during these implosions—the Magneto-Rayleigh-Taylor (MRT) instability on the outer surface of the column and shocks that are launched into the imploding plasma. The dynamics of both features can affect the fusion yield, in the case of MagLIF [see, e.g., Schmit (2016)], and the X-ray or neutron yield of the gas-puff Z-pinch (Jennings, 2015). Consequently, it is important to understand the physics governing both of these effects. This paper describes a set of experiments using a gas-puff Z-pinch to investigate the dynamics of these shocks and the MRT instability in three gasses—neon, argon, and krypton. In particular, we report effects introduced by exchanging the working fluid whilst holding other parameters, including the mass-density in the Z-pinch, constant. Although not the main topic of this paper, it is shown that the highest X-ray yield is produced by the least MRT-unstable implosions.

II. EXPERIMENTAL SETUP AND DIAGNOSTICS

Our gas-puff Z-pinch is generated by the apparatus in Fig. 1, which shows the gas-puff valve with nozzles at cathode potential, the anode-cathode gap of the COBRA 1 MA, 200 ns pulsed-power generator, and a preionizer (Qi, 2014). A piston inside the valve, rapidly actuated by an electromagnetic coil,

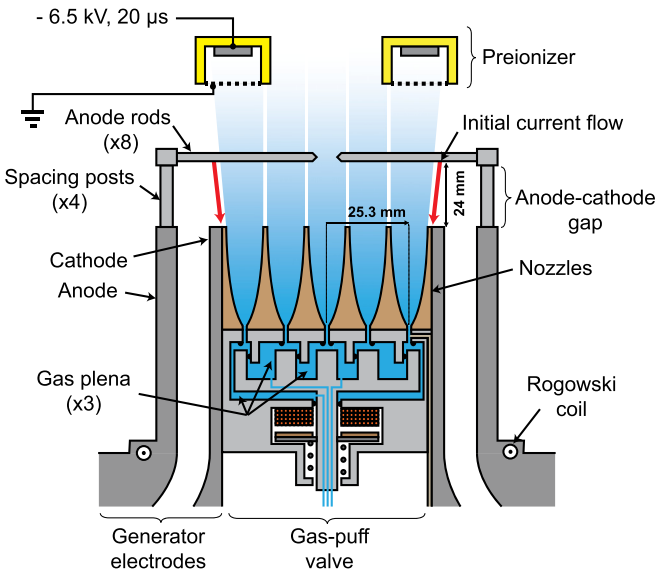

FIG. 1. Gas-puff hardware showing the triaxial valve mounted inside the generator cathode, the anode-cathode gap, and the (grounded) anode surface established by 8 radially orientated rods. An independently driven preionizer mounted above the puff valve ionizes the gas column before the generator current is applied.

[a)]Current address: Naval Research Laboratory, Washington, DC 20375, USA.
[b)]Current address: L-3 Applied Technologies Inc., San Leandro, CA 94577, USA.

releases gas from three independent plena into three concentric nozzles. An approximately cylindrical column of neutral gas is formed in the anode-cathode gap region by the sudden outflow into the high vacuum ($\cong 10^{-2}$ Pa) test chamber. The outer nozzle (O) has a mean radius/aperture width of 25.3 mm/12.5 mm. The inner nozzle (I) has a mean radius/aperture width of 11.3 mm/10.5 mm. The center jet nozzle (J) lies on the cylindrical axis and has a 9 mm aperture. Each of the nozzles injects gas supersonically at Mach numbers exceeding Mach 5, and the outer surface of the outer nozzle material diverges at approximately 5° (de Grouchy *et al.*, 2014).

For experiments discussed in this paper, neon, argon, and krypton were used as working gases and plenum pressures were set in the ratio O:I:J = 1:3:8. This ratio produced a gas puff in the anode-cathode gap that had a relatively flat radial density distribution over the column diameter, modulated by a second order series of density maxima above the nozzle throats (de Grouchy *et al.*, 2014). To ensure that the mass-density injected remained constant in all experiments, absolute pressures for the neon, argon, and krypton experiments were adjusted according to their atomic weights. The absolute pressure in the outer plenum, set at 6.9 ± 0.7 kPa for argon shots, was therefore doubled and halved in neon and krypton experiments, respectively. These pressures resulted in injection of a gas column with an average density of order 1 g m^{-3} into the 24 mm × 70 mm probing region above the nozzles.

The gas-valve nozzles were mounted within the cylindrical high-voltage cathode of the COBRA generator, as shown in Fig. 1. The cathode plane is established by the top surface of the nozzles. Eight 3 mm diameter, radially orientated rods form the anode plane, which was raised above the generator electrodes by a set of four 9 mm diameter spacing posts to provide a 24 mm probing region. After the valve is triggered, but before the COBRA current pulse arrives, the gas is ionized by an independently driven preionizer unit mounted above the anode as shown in Fig. 1. Preionization was necessary to minimize power reflections during early, low-current times of the pulse.

Current traces, recorded using a Rogowski coil mounted around the generator cathode, are shown in Fig. 2 for the 19 shots discussed in this paper. Shot currents generally tracked the mean current profile to within ±15%. In order to simplify the following analysis, the current pulse was modelled using a sine-squared fit

$$I(t) = I_{\max} \sin^2\left(\frac{\pi t}{2t_{rise}}\right), \tag{1}$$

where $I_{\max} = 0.93$ MA and $t_{rise} = 224$ ns are the average peak current and rise time recorded in these experiments, respectively.

The principle diagnostic systems used in these experiments were a 3-channel laser interferometer and two four-frame extreme ultraviolet (XUV) cameras. The laser used for interferometry produced a 150 ps pulse at 532 nm which was split into three beams which were injected at 10 ns intervals to provide both time- and spatially resolved measurements of electron density. The XUV cameras captured system dynamics,

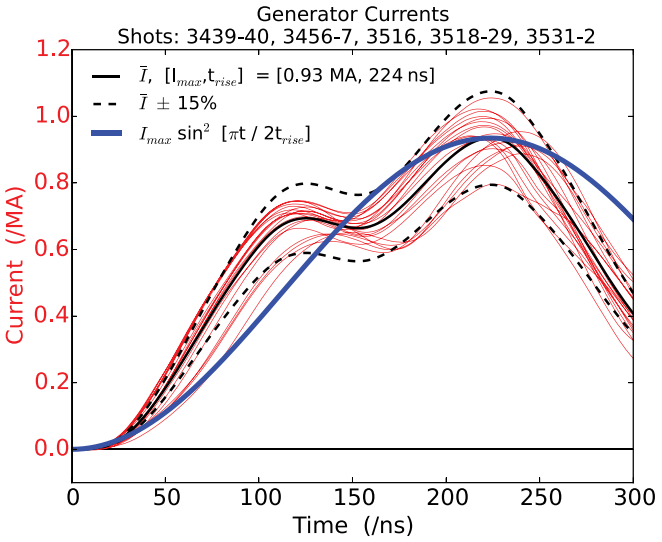

FIG. 2. COBRA current pulses recorded by a Rogowski coil mounted around the generator cathode. Individual current traces (shown in red) illustrate the range of currents observed during these experiments. A sine-squared curve (blue), fitted to the maxima of the average current trace (black), is used for theoretical modelling.

recording emission from the imploding plasma in the $10 < h\nu < 100$ eV spectral band. Two of these cameras were used, and each one produced 4 images, resulting in a sequence of 8 images at 10 ns intervals from each experiment.

III. THEORETICAL MODELS

As the generator current pulse is applied to the ionized gas, the column is compressed by the interaction of the axial current with the self-induced azimuthal magnetic field. We find that the dynamics of this compression agree well with a theoretical model developed by Potter (1978) for Z-pinch compression of a uniform density gas column. Under sufficient magnetic pressure, a compressional wave is launched towards the axis and a strong shock develops. If the current skin-depth is small compared to the column radius, the axial current predominately flows in a thin sheath on the outer surface which acts as a magnetic piston, compressing the material ahead of it. This geometry is shown in Fig. 3(a).

In this figure, axial current flows in the sheath at r_p, the radial position of the piston. The radial position of the shock

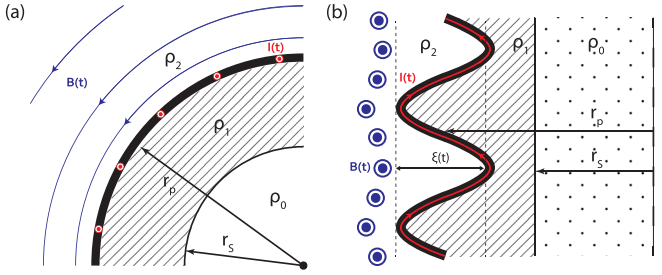

FIG. 3. A simple model of a gas-puff implosion shown from above (a) and in the cross section (b). The self-generated B_θ encloses the current sheath at r_p and an infinitesimally thin cylindrical shock front at r_s. Post-shock gas between r_p and r_s is at higher density ρ_1 than the initial fill density ρ_0. A simple sinusoidal perturbation of the current sheath is shown in (b) representing an ideal MRT instability mode with time-varying peak-peak amplitude $\xi(t)$.

front is r_s. The background fill mass-density is ρ_o, and the densities of the post-shock layer and the chamber vacuum are ρ_1 and ρ_2, respectively, with $\rho_1 > \rho_o > \rho_2$. The shocked material in the shell between r_p and r_s is taken to be moving toward the axis at the same speed as the piston. When both shock and piston positions are large compared to the post-shock layer thickness, they can be calculated numerically, following Potter's formulation of the Rankine-Hugoniot conditions under current-driven magnetic pressure

$$\dot{r}_s(t) = \frac{I(t)}{4\pi r_p(t)}\sqrt{(\gamma+1)\frac{\mu_0}{\rho_0}}, \tag{2}$$

$$\dot{r}_p(t) = \frac{I(t)}{2\pi r_p(t)}\sqrt{\frac{1}{(\gamma+1)}\frac{\mu_0}{\rho_0}}. \tag{3}$$

Here, μ_o is the free-space permeability and γ is the ratio of specific heats.

Numerical solutions to these equations yield the piston and shock positions, velocities, and accelerations, as well as the shock thickness, as functions of time. As an example, Fig. 4 shows solutions for the piston velocity $\dot{r}_p$ and position r_p calculated using Eq. (3) for the simple sinusoidal current given by Eq. (1). The working fluid is an ideal gas, i.e., we have assumed $\gamma = 5/3$. Current flow is initiated at the mean radius of the outer nozzle of 25.3 mm, and a uniform mass-density fill of $\rho_0 = 2.3\,\mathrm{g\ m^{-3}}$ is selected, as inferred from experimental measurements reported in Secs. IV A and V A. Equation (3) is solved at $\Delta t = 0.4$ ns intervals, and each instantaneous velocity $\dot{r}_p(t_i)$ is used to determine the subsequent radial position $r_p(t_i + \Delta t)$. The implosion begins with a low velocity "dwell" phase, proceeds through a long-lived period of gradual acceleration, and concludes with a final compression involving rapid acceleration towards the axis. Note that for $0 < t < 240$ ns—i.e., prior to final compression—piston velocities are reasonably approximated by the average acceleration [$a = 8 \times 10^{11}\ \mathrm{m\ s^{-2}}$].

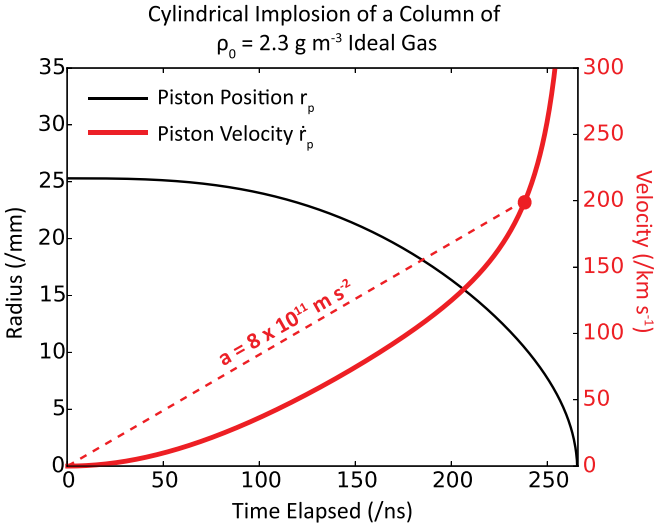

FIG. 4. Numerical solutions for the piston position and velocity as a function of time using the Potter model [Eq. (3)] and the experimentally inferred fill density and initial current sheath position. Note that the ~1 mm post-shock layer thickness observed in our experiments renders the thin shell approximation invalid for $r_p < 10$ mm, i.e., for $t > 240$ ns.

Another feature of these implosions is the Magneto-Rayleigh-Taylor (MRT) instability which develops along the $r = r_p$ surface. Because this interface accelerates inward and separates fluids of different densities $\rho_1 > \rho_2$, it is subject to the unstable MRT perturbation depicted in Fig. 3(b). At a typical Rayleigh-Taylor (RT) unstable boundary—see, e.g., Sharp (1984)—the amplitude ξ of a sinusoidal perturbation of the surface grows exponentially as

$$\xi(t) = \xi_0 e^{\frac{t}{\tau}} \quad \text{with} \quad \tau^{-1} = \sqrt{Aak}. \tag{4}$$

Here, $k = 2\pi/\lambda$ is the wavenumber of the perturbation, ξ_0 is its arbitrary, small initial amplitude, and τ is the time constant associated with its growth. The Atwood number $A = (\rho_1 - \rho_2)/(\rho_1 + \rho_2)$ accounts for the relative fluid densities and goes to unity when $\rho_2 = 0$—the special case of the MRT instability—and to zero if the two fluid densities are equal. Equation (4) describes a simple MRT situation where the amplitude of the perturbation is small compared to its wavelength $\xi(t) \ll k(t)^{-1}$ and densities ρ_1 and ρ_2 are spatially uniform. Although Eq. (4) typically fails to describe large amplitude growth, if, as in our experiments, high density fluid is confined to a thin layer, it may continue to describe growth at large amplitude $\xi(t) > k(t)^{-1}$ [see, e.g., Liberman (1999)].

Livescu (2004) has recently studied the effects of compressibility, viscosity, and density variations on the Rayleigh-Taylor (RT) growth rate and reconciled conflicting theoretical studies in this area. Of particular relevance to our experiments, he concludes that an exponential density variation within the material ahead of the piston—i.e., between r_p and r_s—can reduce the effective Atwood number in Eq. (4) to $\ll 1$, effectively suppressing RT growth. We observe a uniform post-shock radial density profile in argon experiments [i.e., $\rho_1(r) = const.$], while in krypton, this profile is exponential-like. As will be shown, RT growth rates are strongly suppressed in krypton shots, in qualitative agreement with Livescu's theory.

IV. NEON IMPLOSIONS

Neon implosions were produced using an O:I:J pressure ratio of 1:3:8, with the outer plenum at an absolute pressure of 13.8 kPa. This configuration produced an approximately uniform density column with an average mass-density of $2.3\,\mathrm{g\,m^{-3}}$ in the 24 mm inter-electrode gap. These implosions were studied using two XUV ($10 < h\nu < 100$ eV) four-frame cameras. Each camera contained four, 200 μm diameter pinhole apertures that were aligned to place images of the imploding plasma column onto four electrically isolated quadrants of a microchannel plate (Bland, 2004). The quadrants were triggered at 10 ns intervals, and the second camera was triggered approximately 40 ns after the first. The two cameras were mounted at 15° azimuthal separation—as closely as possible on the test chamber—so that individual flow features could be tracked across both sets of images. The result was 8 XUV images covering a 70 ns observation window, as shown as an example in Fig. 5. These images

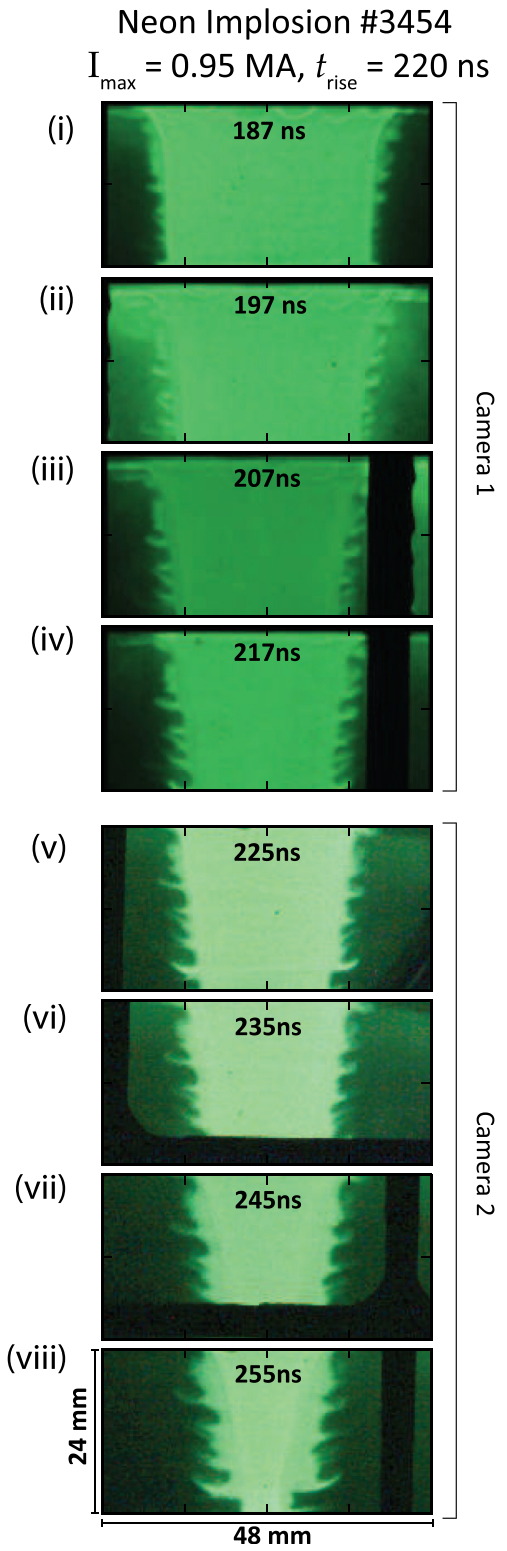

FIG. 5. An example set of XUV images from a neon implosion. Two cameras each capture four frames at 10 ns intervals. Here, camera 2 followed the first after an additional 8 ns. Images, cropped at the electrode surfaces, show the full 24 mm length of the anode-cathode gap.

provide almost no information regarding dynamics inside the column, but the sharp outer boundary can be used to determine r_p and the MRT perturbation wavelength $\lambda(t)$ and amplitude $\xi(t)$, and hence the time constant τ associated with its growth.

A. Radial implosion

An average vacuum/plasma interface position is computed across the column length for each of the images in Fig. 5 to produce the plot of the average column radius vs. time shown in Fig. 6. Error bars represent the uncertainty associated with determining the exact radial position of the boundary at each sampled point. Results are compared to theoretical implosion trajectories generated using Eq. (3). We find that the average radial position of the column surface is well matched to first order by the model trajectory generated using a $2.3\,\mathrm{g\,m^{-3}}$ average fill density and the mean outer nozzle radius of $r_o = 25.3\,\mathrm{mm}$ as the initial current position. A second-order sequence of acceleration, deceleration, and re-acceleration can be observed, consistent with the shell traversing a region of higher fill-density above the inner nozzle throat (de Grouchy *et al.*, 2014). Some estimate of the sensitivity of the model fit to changes in the fill-density and initial radius is provided by contours of $\rho_0 \pm 10\%$ and $r_0 \pm 5\%$, respectively. The reasonable fit between the column radius and the simple implosion model suggests that a uniform acceleration of $a = 8 \times 10^{11}\,\mathrm{m\,s^{-2}}$ sufficiently accounts for first-order dynamics observed during the gradual acceleration phase.

B. The MRT instability

If the images shown in Fig. 5 are expanded, the effect of the MRT instability can be observed, generating ripples on the vacuum/plasma interface which grow in time. Figure 7 shows an expanded image of the column at 197 ns. The evolution of the ripples is quantified by tracking turning points in the XUV images along the vacuum/plasma interface as illustrated in Fig. 7. These turning points are selected by eye, at positions along the boundary separating brightly emitting plasma from low emission vacuum regions where the tangent to the surface lies parallel to the column axis. The clear identification of MRT minima ("bubbles") and maxima ("spikes") is made possible by the strong azimuthal symmetry observed

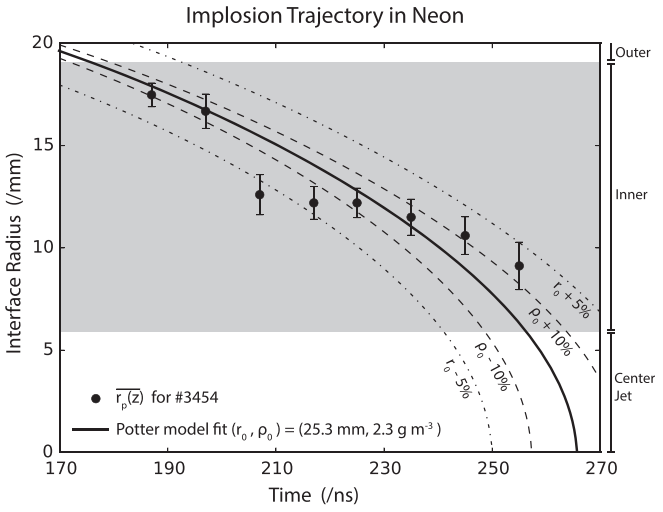

FIG. 6. Average vacuum/plasma boundary position vs. time for the neon implosion shown in Fig. 5. The best-fit theoretical implosion trajectory generated using Eq. (3) suggests an initial current sheath radius of 25.3 mm and an average fill density of $2.3\,\mathrm{g\ m^{-3}}$—values consistent with the geometry and capacity of our gas-puff.

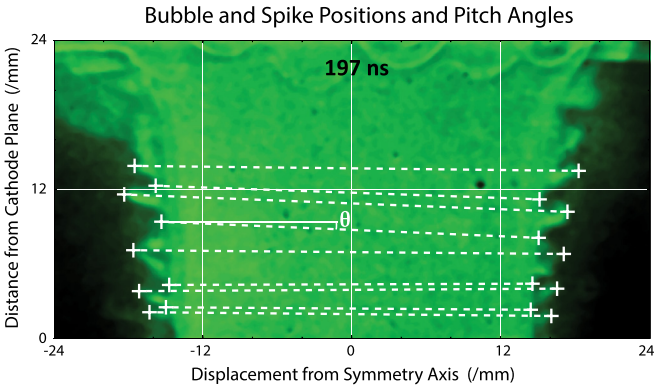

FIG. 7. XUV image (ii) from Fig. 5 expanded to show deformation of the plasma/vacuum boundary due to the MRT instability. Maxima and minima, indicated by crosshairs, are used to compute the average boundary position and perturbation wavelength/amplitude. The one-to-one correlation between extrema on both sides of the column reflects the azimuthal symmetry observed during the gradual acceleration phase.

during these implosions. This symmetry is illustrated in Fig. 7 by the one-to-one relationship between extrema observed on opposite surfaces of the column—the average pitch angle of the 9 marked pairs is less than 2° from the horizontal. Note that the upper 6 mm of the column is in general excluded from the following analysis since end effects (including the formation of bow shocks around the anode rods as visible in Fig. 7) in this region significantly disrupt column symmetry and hence MRT evolution.

The average MRT wavelength $\lambda(t)$ at each image time is determined by counting the total number of ripple periods in the sampled axial length. The time evolution of this average wavelength is plotted in Fig. 8(a) for 180–260 ns. The standard deviation of the individual wavelengths observed along the sample length provides a first-order estimate of the uncertainty associated with these averages. There is little variation in the average wavelength, and to within 10%, it remains steady at $\overline{\lambda(t)} = 2.9$ mm.

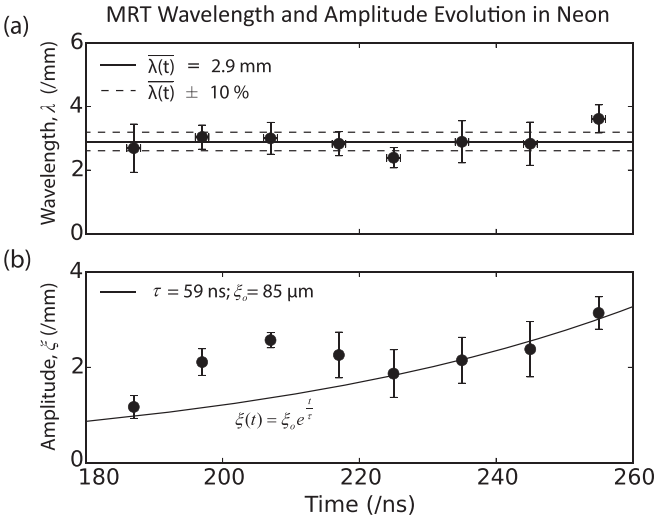

FIG. 8. Average values of the MRT wavelengths (a) and peak-peak amplitudes (b) observed along the vacuum/plasma boundary at each XUV image time. The sample size for each average is 16 - eight half-wavelengths measured on either side of the plasma column.

The average peak-peak amplitude ξ of the perturbation at each image time is calculated by averaging the set of radial displacements between pairs of adjacent turning points. The growth curve that results is plotted in Fig. 8(b). The wavelength error bars represent the standard deviation of the amplitudes recorded along the column. Using the steadily increasing late-time data (i.e., $t > 220$ ns) to determine an exponential fit, we find that a time constant $\tau = 59$ ns produces an excellent fit to the data if the three data points $190 < t < 220$ ns are excluded. It is possible that supplementary growth here is due to the burst of additional acceleration observed in Fig. 6, as the shell traverses the lower-density material above the inner nozzle wall. Although this growth rate is close to the $\tau = 24$ ns value predicted by Eq. (4) with A = 1 (for the ideal MRT instability), it is a factor of 2.4 slower, suggesting an effective Atwood number of 0.17. Experimentally measured Atwood numbers less than 1 will be discussed in Sec. V B.

V. ARGON AND KRYPTON IMPLOSIONS

For this series of measurements, implosions in argon and krypton were studied, holding mass-density constant. The laser interferometer was used to probe details of shock dynamics inside the column. The laser pulse injected in each experiment was 150 ps long and frequency doubled to 532 nm. In argon experiments, interferometry was performed in the Mach-Zehnder (MZ) arrangement (Hutchinson, 2002) in which the deflection of fringes is proportional to line-integrated electron density at each image position. In krypton, small-shift shearing (SSS) interferometry (Pikuz, 2001) was used, in which fringe deflections reflect the difference in line-integrated electron densities between each image position and a position horizontally displaced by 0.5 mm. The plenum pressure ratio was maintained at O:I:J = 1:3:8 for radially uniform puffs. For argon experiments, the outer plenum was charged to 6.9 kPa, resulting in an average fill density of 2.3 g m^{-3}. For krypton shots, the absolute plena pressures were reduced by a factor of 2 to maintain the same mass-density.

A. Radial density profiles from interferometry

Typical interferometry data are shown in Fig. 9 alongside axial vs. radial electron density plots extracted from each image. Strong fringe shifts, indicating high electron densities, are apparent between $9 < r < 12$ mm for argon and $r < 9$ mm for krypton. Interpolating between fringes (Swadling, 2013) and performing an Abel inversion about the Z-axis (Hutchinson, 2002) returns the electron density plots shown underneath the fringe-shift data. The three regions ρ_0, ρ_1, and ρ_2 suggested by Potter's uniform density Z-pinch model (see Sec. III) are readily identified, with relative densities $\rho_1 > \rho_o > \rho_2$ as expected.

Consistency with Potter's model in argon is confirmed by radial profiles taken across these electron density maps. Two such profiles, averaged over 1 mm axial lengths centered on MRT bubbles and spikes at positions marked in Figs. 9(c) and 9(d), are shown in Fig. 10. The locations of the vacuum/plasma boundary r_p and the forward shock r_s, as

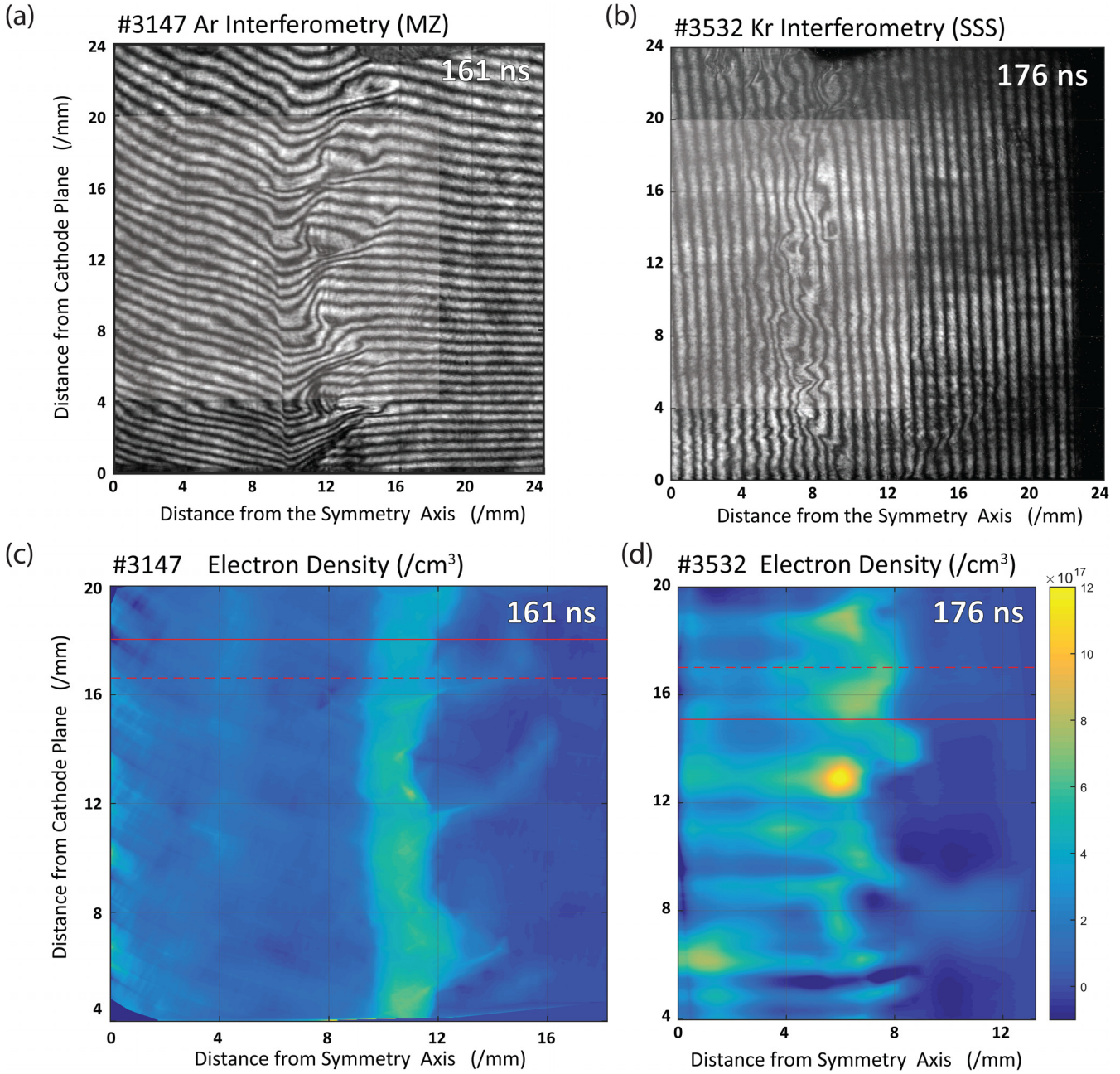

FIG. 9. Interferometry results for argon (a) and krypton (b) implosions captured halfway through the XUV observation window. Deflected interference fringes are shown in the upper images, and the corresponding values for the electron density vs. radius are shown below in images (c) and (d), respectively. The axial positions of radial profiles shown in Fig. 10 are marked in figures (c) and (d) red.

well as the radial profiles in the region between them, are very different for the two gasses. For argon, the density is uniform in the post-shock layer and fronted by a narrow shock. For krypton, no clear forward shock is observed—rather, the density increases gradually with the radius. Along with this difference in the radial density profiles, it will be shown that the argon and krypton implosions have very different MRT growth rates, in agreement with Livescu's computational results (Livescu, 2004).

Figure 11 shows $r_p(t)$, the position of the vacuum/plasma boundary, for argon and krypton implosions, as determined from XUV images using the method outlined for Ne shots in Sec. IV. Since the mass-density is held constant, Eq. (3) suggests that both implosions should follow identical trajectories, with the same average accelerations, save for the $\pm 15\%$ uncertainty introduced by variable machine current. The solid line in this figure is generated by the solution to Eq. (3) for $\rho_o = 2.3\,\mathrm{g\,m^{-3}}$ and $r_p(0) = 20\,\mathrm{mm}$. An average acceleration of $a = 1.0 \times 10^{12}\,\mathrm{m\,s^{-2}}$ is experienced along this trajectory for the first 180 ns of the implosion, during which time $r_p > 10\,\mathrm{mm}$ and the thin layer approximation holds. This fit provides a reasonable first approximation for both Ar and Kr data. The best fit for krypton suggests a slightly smaller initial current radius of $r_o = 19.4\,\mathrm{mm}$, while the argon data fit best with a marginally larger starting radius of $r_o = 20.6$ mm. It seems likely that the lower number density in Kr puffs may result in the current sheath initializing at a smaller radius. Indeed, both Ar and Kr fits suggest smaller

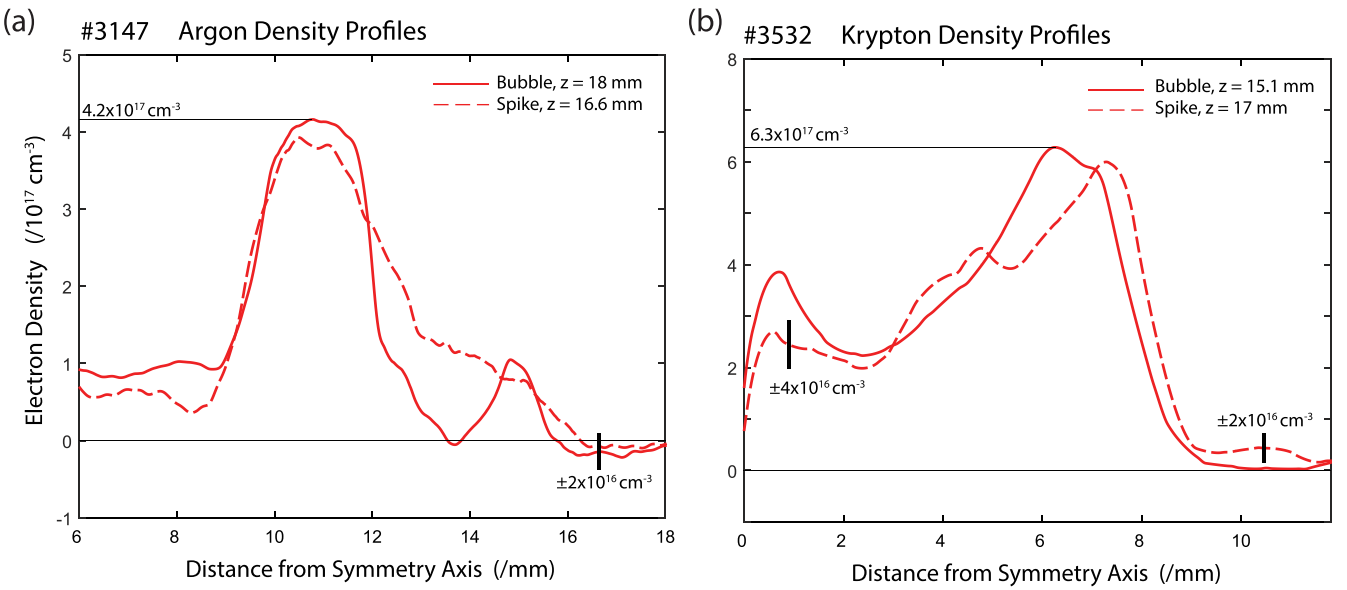

FIG. 10. Radial electron density profiles in argon (a) and krypton (b). Profiles are centered along MRT bubbles and spikes as indicated by solid and dashed lines respectively. Uncertainties due to finite interference fringe thickness are compounded at small radii by computational errors introduced during the Abel inversion by assuming an exact symmetry axis position.

initial sheath radii than observed for Ne puffs (Sec. IV) for which number densities are higher.

B. MRT growth rates

While the effect of the MRT instability on the vacuum/plasma boundary can be seen in the interferometry data of Fig. 9, a quantitative analysis of the interface is more accurately performed using XUV quadrant camera images and the approach outlined in Sec. IV. Similar measurements to those shown in Figs. 5 and 7 were performed and analyzed for argon and krypton implosions. The resulting average perturbation wavelengths and amplitudes for the two implosions analyzed in Figs. 9–11 are shown as functions of time in Fig. 12. As for Ne results, error bars represent the spread of wavelengths and amplitudes observed along the sampled

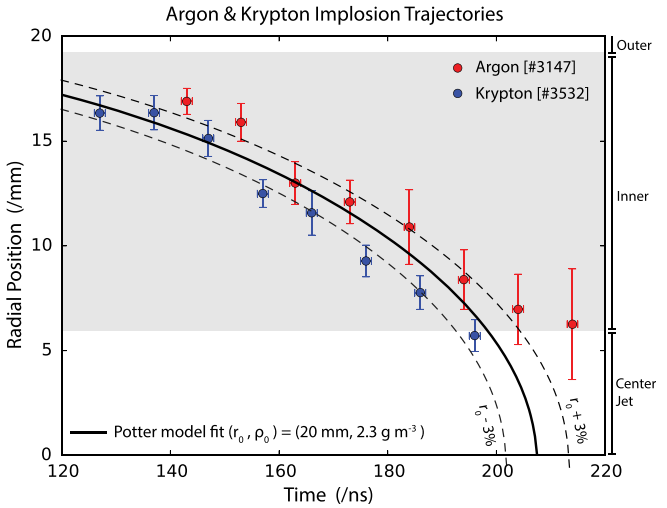

FIG. 11. Average vacuum/plasma boundary position in argon (red) and krypton (blue) implosions, extracted from XUV images of the shots imaged in Fig. 9. Theoretical fits are generated using Eq. (3).

axial length. Although there is some second-order evidence of wavelength variation, both Ar and Kr wavelengths are generally consistent with a steady average of 3.5 mm and 3.1 mm, respectively. The time constant $\tau = 53$ ns describing the MRT growth in argon is close to the 24 ns classical result obtained using an acceleration of $a = 1.0 \times 10^{12}\,\mathrm{m\,s^{-2}}$, a wavelength of 3.5 mm, and an Atwood number of $A = 1$. It is interesting to note how similar this time constant is to the 59 ns best fit to our Ne data. A comparable effective Atwood number $A = 0.21$ is suggested by Eq. (4) for argon implosions.

Although the krypton and argon shells imploded with near-identical accelerations, MRT growth in krypton was significantly suppressed. Although measurable perturbation amplitudes were recorded from the earliest observation times, no significant change in the 1.4 mm initial amplitude was observed across the $120 < t < 220$ ns observation window. Indeed, fitting an exponential curve to the data returns an unfeasibly large time constant $\tau = 1$ μs and an implausible seed amplitude $\xi_0 = 1.2$ mm. Given the similarity between Ne and Ar growth rates, and the more reasonable 100 μm initial amplitudes suggested for both by best fit growth curves, it seems likely that similar early-time growth occurred in Kr which was capped at 1.4 mm before our earliest probing time. Looking back to Fig. 10, it can be seen that, in contrast to argon experiments, krypton density in the layer of the high-density imploding material varies quasi-exponentially at t = 176 ns—i.e., by the middle of our observation window. Livescu's theoretical analysis of MRT growth rates in fluids of exponentially varying density (Livescu, 2004) predicts strong suppression of growth when the MRT wavelength is similar to or larger than the density e-folding length. Even at this relatively late time, the 3.5 mm full width of the krypton layer barely exceeds the 3.1 mm average MRT wavelength. Thus, the observed MRT suppression in krypton experiments is qualitatively consistent with Livescu's theoretical model.

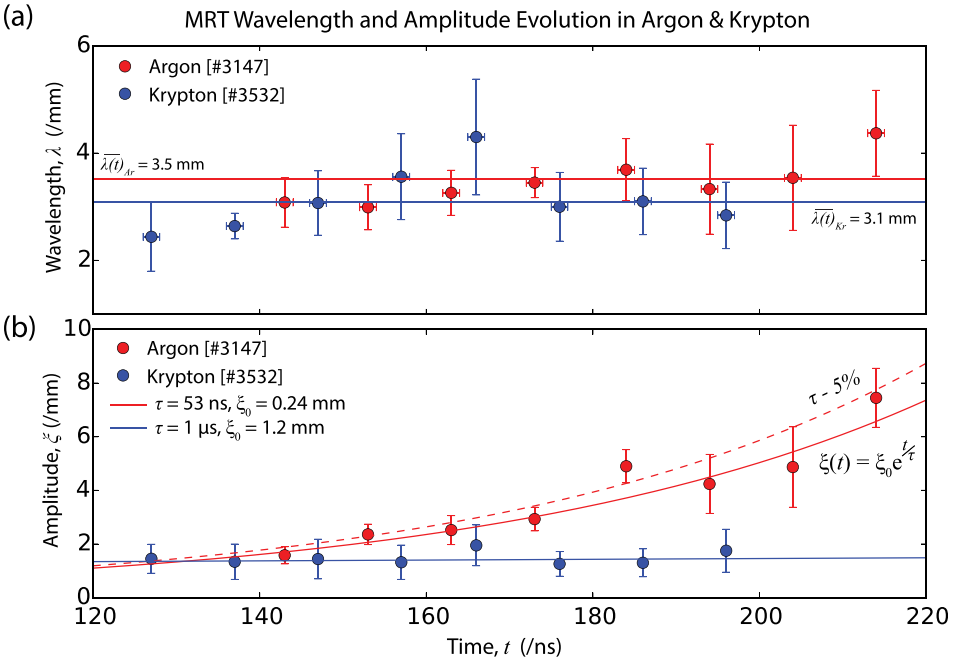

FIG. 12. Average MRT wavelengths (a) and amplitudes (b) measured in argon (red) and krypton (blue) shots using XUV images. Constant wavelength fits and exponential growth curves produce reasonable agreement with wavelength and amplitude data, respectively, except in the case of krypton amplitudes, where no significant growth is observed.

C. X-rays

One of the primary applications of the gas-puff Z-pinch is as an intense X-ray source. While X-ray production was not the main focus of these experiments, some measurements of the overall yield were performed. Intense X-ray bursts that occurred when the imploding plasma stagnated along the cylindrical axis were measured using filtered photoconducting detectors (PCDs) (Spielman, 1995). Traces from a 4 μm polypropylene-filtered PCD fielded on argon and krypton experiments nominally identical to those discussed above are shown in Fig. 13. This filter has transmission windows between $100 < h\nu < 300$ eV and $h\nu > 400$ eV, and detector volts are proportional to total radiative power transmitted onto the photoconductive element. An estimate of the relative X-ray yield in these bands can thus be determined from the integrated area between the signal and the detector rest state.

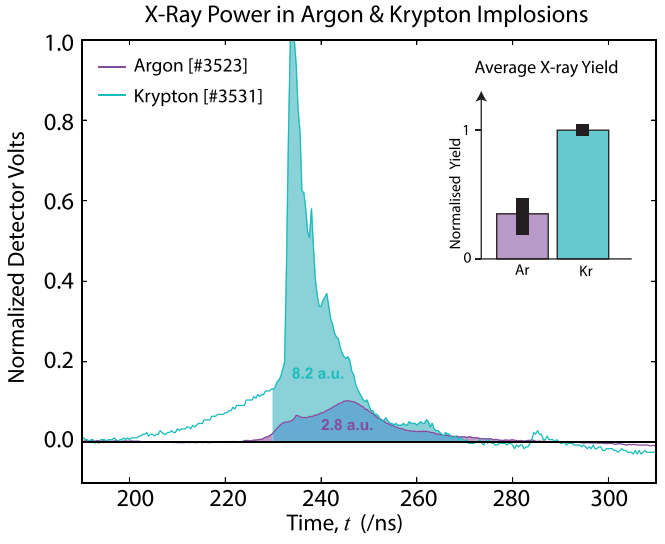

FIG. 13. X-ray power vs. time for argon (purple) and krypton (blue) implosions as captured by a 4 μm polypropylene-filtered photoconducting detector. Shaded areas are proportional to total x-ray energy emitted when imploding plasma stagnates along the cylindrical axis. The average yield recorded in the eight argon experiments is shown in the subplot, normalized against the average yield recorded in the three krypton implosions.

X-ray yields were calculated in this way for all 11 argon and krypton experiments. Pre-stagnation radiation—i.e., radiation recorded before the sharp leading edge of the signal—is excluded from these calculations. Average yields for the two gases are shown in Fig. 13 (inset) in arbitrary units, normalized against the average Kr yield. Error bars represent the spread of yields recorded in the eight Ar and three Kr experiments. It can be seen that the more MRT-stable krypton implosions produced a more consistent and intense X-ray burst than otherwise identical argon implosions, delivering 2.9 times higher yields in our observation bands.

VI. SUMMARY AND CONCLUSIONS

We have studied the cylindrical shocks launched towards the symmetry axis during gas-puff Z-pinch implosions in neon, argon, and krypton and the Magneto-Rayleigh-Taylor (MRT) instability of the vacuum/plasma boundary in each case. By imaging the plasma column at eight evenly spaced instants during each experiment, we have tracked the changing position r_p of this surface across each implosion. In all three gases, we find that boundary positions recorded during our 70 ns observation window agree to first-order with theoretical implosion trajectories determined using Potter's (Potter, 1978) equations of motion for a Z-pinch in uniform-density gas. This model treats the Z-pinch current as confined to an infinitesimally thin sheath at the vacuum/plasma boundary. Best fits to our data suggest that such a sheath forms during our experiments, but at different initial radii in the three gases—directly above the outer nozzle in neon implosions—and at smaller radii in argon and krypton. It is likely that the lower number-densities in our argon and krypton gas-puffs are responsible for this effect.

The vacuum/plasma boundary was observed to be MRT unstable, and the average perturbation wavelengths and peak-peak amplitudes were measured at each probing time. Similar average wavelengths of around 3 mm were observed in all three fluids, and no significant changes in the wavelength were recorded during our observation window. Perturbation amplitudes were found to grow exponentially in neon and argon experiments, with time constants of 59 ns and 53 ns, respectively. Average accelerations of 8.0×10^{11} m/s^2 and 1.0×10^{12} m/s^2 suggested by best fit implosion trajectories indicate that neon and argon implosions can be characterized by similar effective Atwood numbers—$A = 0.17$ and $A = 0.21$, respectively. Atwood numbers less than unity could be the consequence of current migration into the post-shock plasma,—moving the effective radius of the unstable boundary to some position within the imploding material. This situation is possible in COBRA gas-puff Z-pinches where skin-depths can exceed 1 mm if plasma temperature is sufficiently low.

In order to compare the MRT instability growth rates in the different working gases, care was taken to ensure that puffs in neon, argon, and krypton were initialized with similar average mass-density and radial mass-density profiles. Although similar MRT wavelengths to those recorded in neon and argon were observed in krypton experiments, no significant increase in krypton MRT amplitude was recorded within our observation window. Measurements of electron density revealed that a localized, stable cylindrical shock was launched in argon implosions, fronting a uniform-density plasma layer between the shock and the vacuum/plasma boundary. No such forward shock was observed in krypton experiments, and the layer of imploding plasma was found to decay quasi-exponentially from the vacuum/plasma boundary towards the axis. Livescu (2004) has theoretically studied the effects of mass-density variation on the Rayleigh-Taylor growth rate. In particular, he has predicted that exponentially varying mass-density on either side of an unstable interface is capable of suppressing RT growth when the mass-density e-folding length is equivalent to or smaller than the dominant RT wavelength. This prediction is consistent with the suppression of MRT growth we have observed in krypton experiments where the 3.5 mm measured layer thickness is similar to the 3.1 mm average MRT perturbation wavelength. X-ray bursts recorded in more stable krypton implosions produced 2.9 times higher yields than in less stable argon implosions.

ACKNOWLEDGMENTS

This work was supported by the National Nuclear Security Administration's Stewardship Sciences Academic Programs under the Department of Energy Cooperative Agreement No. DE-NA0001836. The triaxial valve was designed and manufactured by the Weizmann Institute of Science Plasma Laboratory's gas-puff team. The authors also thank Drs. Sergei Pikuz, Tania Shelkovenko, and John Greenly for helpful discussions and advice. The experimental equipment was maintained and operated by the technical team—Messrs Harry Wilhelm, Todd Blanchard, Daniel Hawkes and Dr. William Potter.

Bland, S. N., Ampleford, D. J., Bott, S. C., Lebedev, S. V., Palmer, J. B. A., Pikuz, S. A., and Shelkovenko, T. A., "Extreme ultraviolet imaging of wire array z-pinch experiments," Rev. Sci. Instrum. **75**, 3941–3943 (2004).

de Grouchy, P. W. L., Rosenberg, E., Qi, N., Kusse, B. R., Kroupp, E., Fisher, A., Maron, Y., and Hammer, D. A., "Characterization of the COBRA triple-nozzle gas-puff valve using planar laser induced fluorescence," AIP Conf. Proc. **1639**(1), 43–46 (2014).

Giuliani, J. L. and Commisso, R. J., "A review of the gas-puff Z-pinch as an X-ray and neutron source," IEEE Trans. Plasma Sci. **43**(8) 2385–2453 (2015).

Hutchinson, I. H., *Principles of Plasma Diagnostics*, 2nd ed. (Cambridge University Press, 2002).

Jennings, C. A., Ampleford, D. J., Lamppa, D. C., Hansen, S. B., Jones, B., Harvey-Thompson, A. J., Jobe, M., Strizic, T., Reneker, J., Rochau, G. A., and Cuneo, M. E., "Computational modeling of Krypton gas puffs with tailored mass density profiles on Z," Phys. Plasmas **22**(5), 056316 (2015).

Liberman, M. A., De Groot, J. S., Toor, A., and Spielman, R. B., *Physics of High-Density Z-Pinch Plasmas* (Springer-Verlag, New York, Inc., 1999).

Livescu, D., "Compressibility effects on the Rayleigh-Taylor instability growth between immiscible fluids," Phys. Fluids **16**(1), 118–127 (2004).

Pikuz, S. A., Romanova, V. M., Baryshnikov, N. V., Hu, M., Kusse, B. R., Sinars, D. B., Shelkovenko, T. A., and Hammer, D. A., "A simple air wedge shearing interferometer for studying exploding wires," Rev. Sci. Instrum. **72**(1), 1098–1100 (2001).

Potter, D., "The formation of high-density Z-pinches," Nucl. Fusion **18**(6), 813 (1978).

Qi, N., Rosenberg, E. W., Gourdain, P. A., de Grouchy, P. W. L., Kusse, B. R., Hammer, D. A., Bell, K. S., Shelkovenko, T. A., Potter, W. M., Atoyan, L., Cahill, A. D., Evans, M., Greenly, J. B., Hoyt, C. L., Pikuz, S., Schrafel, P., Kroupp, E., Fisher, A., and Maron, Y., "Study of gas-puff Z-pinches on COBRA," Phys. Plasmas **21**(11), 112702 (2014).

Schmit, P. F., Velikovich, A. L., McBride, R. D., and Robertson, G. K., "Controlling Rayleigh-Taylor instabilities in magnetically driven solid metal shells by means of a dynamic screw pinch," Phys. Rev. Lett. **117**(20), 205001 (2016).

Sharp, D. H., "An Overview of Rayleigh-Taylor Instability," Phys. D: Nonlinear Phenom. **12**(1-3), 3–18 (1984).

Slutz, S. A. and Vesey, R. A., "High-gain magnetized inertial fusion," Phys. Rev. Lett. **108**(2), 025003 (2012).

Spielman, R. B., "Diamond photoconducting detectors as high power z-pinch diagnostics," Rev. Sci. Instrum. **66**(1), 867–870 (1995).

Swadling, G. F., Lebedev, S. V., Niasse, N., Chittenden, J. P., Hall, G. N., Suzuki-Vidal, F., Burdiak, G., Harvey-Thompson, A. J., Bland, S. N., De Grouchy, P., Khoory, E., Pickworth, L., Skidmore, J., and Suttle, L., "Oblique shock structures formed during the ablation phase of aluminum wire array Z-pinches," Phys. Plasmas **20**(2), 022705 (2013).